





## First-principles study of spin spirals in the multiferroic BiFeO<sub>3</sub>

Bin Xu <sup>1,2,\*</sup>, Sebastian Meyer <sup>3,\*</sup>, Matthieu J. Verstraete <sup>3</sup>, Laurent Bellaïche,<sup>2</sup> and Bertrand Dupé <sup>3,4</sup>

<sup>1</sup>Jiangsu Key Laboratory of Thin Films, School of Physical Science and Technology, Soochow University, Suzhou 215006, China

<sup>2</sup>Physics Department and Institute for Nanoscience and Engineering, University of Arkansas, Fayetteville, Arkansas 72701, USA

<sup>3</sup>Nanomat/Q-mat/CESAM and European Theoretical Spectroscopy Facility, Université de Liège, B-4000 Sart Tilman, Belgium

<sup>4</sup>Fonds de la Recherche Scientifique (FNRS), Bruxelles, Belgium



(Received 13 January 2021; revised 1 May 2021; accepted 24 May 2021; published 11 June 2021)

We carry out density functional theory (DFT) calculations to explore the antiferromagnetic (AFM) spin cycloid in multiferroic BiFeO<sub>3</sub> of the *R3c* ground state structure. We calculate the energy dispersion  $E(\mathbf{q})$  of cycloidal spin spirals along the high symmetry directions of the pseudo-cubic unit cell and find a flat AFM spin spiral (or cycloid) ground state with a periodicity of  $\sim 80$  nm, which is in good agreement with experiments. To investigate which structural distortion of the *R3c* phase is the driving mechanism for the stabilization of this cycloid, we further study three artificial phases: *cubic*,  $\bar{R}3c$ , and *R3m*. In all cases, we find a large exchange frustration. The comparison between these phases provides detailed insight about how polarization and octahedral antiphase tilting affect the different magnetic interactions and the magnetic ground state in BiFeO<sub>3</sub>. In *R3c* BiFeO<sub>3</sub>, the magnetic ground state is driven by a competition between the frustrated exchange stemming from the hybridization between the elements Bi, Fe, O and the Dzyaloshinskii-Moriya (DM) interaction due to the Fe-Bi ferroelectric displacement. The cycloid appears to be stable because the anisotropy energy in *R3c* BiFeO<sub>3</sub> is relatively small to enforce a collinear order.

DOI: [10.1103/PhysRevB.103.214423](https://doi.org/10.1103/PhysRevB.103.214423)

### I. INTRODUCTION

BiFeO<sub>3</sub> (BFO) is one of the few single-phase room-temperature multiferroics which exhibit a large spontaneous polarization. BFO has an antiferromagnetic texture that can be approximated locally by a G-type order (G-AFM) in its *R3c* ground state. Its Curie temperature is 1123 K [1] and its Néel temperature is 643 K. The *R3c* structure has a polarization of about  $90 \mu\text{C}/\text{cm}^2$  at low temperature [2], arising from off-centered ionic displacements along the [111] direction, and also shows antiphase antiferrodistortive (AFD) oxygen octahedral tiltings ( $a^-a^-a^-$  in Glazer's notation [3]). In the bulk form, the AFM order is modified by the presence of the Dzyaloshinskii-Moriya (DM) interaction [4,5], which creates a spin cycloid [6] that propagates along the [110] direction, with magnetic moments lying in the plane formed by the polarization and the propagation direction. The periodicity of the spiral is 62 nm [7,8].

The DM interaction originates from spin-orbit coupling (SOC). It is typically understood as the magnetic interaction between two magnetic atoms mediated by an electron which is under the influence of SOC [9]. Additionally, in multiferroics the internal electric field has been identified as a possible source of DM interaction [10]. In BFO both effects could add to each other: The *d* orbitals of Bi could induce a strong SOC [11] and the structural distortions could generate an internal SOC, specifically through polar displacements, that create an internal dipole and break inversion symmetry [12,13], or AFD tilts that mediate the magnetic superexchange interaction

[14,15]. The former DM interaction has a magnetoelectric nature and is crucial to explain the stabilization mechanism of the spin spiral, as it favors chiral magnetic noncollinear configurations, while the latter DM interaction is responsible for the spin density wave (or cycloidal tilt) [16] or weak magnetization in the absence of the magnetic cycloid [14]. The presence of a DM interaction driven spin cycloid in BFO has triggered many works over the last ten years because it enables electromagnon coupling [17–19] and couples to polarization and strain [19–21].

Although of considerable interest, the cycloid of BFO was only recently explored numerically in Ref. [22]. Since the periodicity of 62 nm is too large to be studied fully from first principles, its exploration had to rely on the parametrization of a Heisenberg Hamiltonian based on the four-state energy mapping method. The exploration of the different magnetic configurations is then carried out via Monte Carlo simulations [22]. This method gives AFM spin cycloid ground state properties, and the resulting cycloidal pitch of 83 nm was found in good agreement with experiment. However, this method does not allow for the direct assessment of the stability of the cycloid, in particular if long-range exchange interactions are important, and hence, lacks a description of the different stabilization mechanisms that only microscopic electronic structure calculations could provide.

A suitable method to address this task is the calculation of incommensurate spin spirals [6]. These have a much larger magnetic unit cell as compared with the chemical unit cell and have been studied theoretically for more than twenty years in ferromagnetic materials. In metals, significant efforts have been made to simulate noncollinear magnetic states based on the chemical unit cell [23]. This approach is known as

\*These authors contributed equally to this work.

the generalized Bloch theorem and relies on the modulation of the phase of the electron spinors by a factor  $\pm\mathbf{q}/2$  for up and down spin, respectively. The framework allows the calculation of all incommensurate magnetic spin spirals in the first Brillouin zone, at a cost which corresponds to a single chemical unit cell.

This approach has been extended to explore the SOC contribution to the total energy of the spin spiral [24]. In this case, SOC is included in the perturbation theory and gives access to the DM interaction. It has been very successful in describing noncollinear magnetic states at surfaces or interfaces, which are stabilized by the DM interaction in rather simple crystallographic geometries where the model of Levy and Fert directly applies [9]. This method has the advantage of quantifying the source of the DM interaction in terms of SOC contribution to the total energy. It has been central to obtain key knowledge in the fields of chiral spintronics where it could identify the 5*d*-transition metal substrate [25,26], the interfacial electric field [27,28], or the oxygen concentration at surfaces [29] as a source of the DM interaction. Although this methodology is now standard for metals, it has never been applied to magnetic multiferroic oxides.

In the case of the multiferroic BFO, including the DM interaction is crucial as it is responsible for the stabilization of the spin cycloid [30], as well as the weak (ferro)magnetization due to spin canting [14,31,32]. It is also central to the mechanism for the magnetoelectric (ME) coupling [33]. As compared with metals, the crystal structure of a multiferroic oxide is of prime importance to accurately describe its physical properties. For example, in a multiferroic of the ABO<sub>3</sub> type, the crystallographic structure must be correctly reproduced to obtain good transport and magnetic properties [34].

For BFO, the DM interaction may occur through different mechanisms. The coupling between the magnetic moments on neighboring sites is mediated by an oxygen atom which locally breaks inversion symmetry (via octahedral tilts). This mechanism occurs via the superexchange and could be enhanced via the SOC of the *p* orbitals of oxygen [10]. In that case, the direction of the DM interaction should be perpendicular to the Fe-O-Fe planes. Another mechanism may involve the bismuth atoms, which break inversion symmetry via the ferroelectric distortions [11]. This mechanism, also known as the spin current model, creates a DM interaction perpendicular to the polarization and spiral propagation direction. In that case, the *p* orbitals of bismuth, which hybridize with the *d* orbitals of iron, could enhance the DM interaction. Finally an internal electric field is created by the off-centered ferroelectric displacements (involving bismuth, iron, and oxygen). In that case, the DM interaction would be favored in a plane perpendicular to the potential gradient [35], e.g., to the  $\langle 111 \rangle$  directions.

Since both the positions of the oxygen and the bismuth may affect the amplitude and direction of the DM interaction, several phases should be explored to probe the origin of the DM interaction. This also opens up the possibility that changing the crystal structure of the ABO<sub>3</sub>-type multiferroic will change the DM interaction and therefore also the propagation of the spin cycloid [36].

In this paper, by means of state-of-the-art density functional theory (DFT) calculations, we study the incommensu-

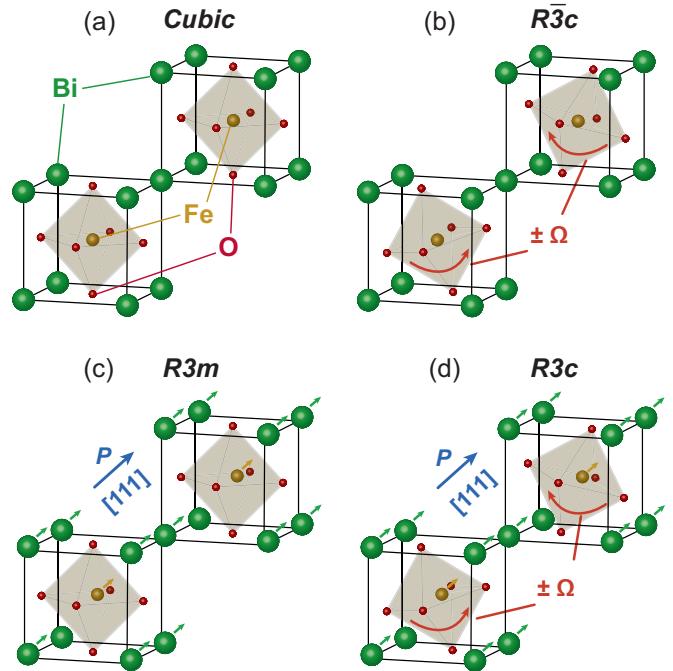


FIG. 1. Sketches of the studied BiFeO<sub>3</sub> structures. Green spheres correspond to the Bi atoms, golden spheres in the center of each cube denote Fe, and small red spheres show O atoms. (a) Centrosymmetric *cubic* structure, (b)  $R\bar{3}c$  structure where only the oxygen octahedral tilts are included, represented by curved arrows and  $\pm\Omega$ . (c)  $R3m$  structure, where only the ferroelectric displacement is included, denoted by arrows at the Bi sites and Fe sites. The displacement leads to a large spontaneous polarization  $P$  in the  $[111]$  direction. (d) Structural  $R3c$  ground state where both effects, oxygen octahedral tilts from (b) and ferroelectric displacement from (c), are included. Note that the structures of (a)–(c) are artificial to isolate the structural distortions of the  $R3c$  phase.

rate spin cycloid in BFO. To explain the magnetic structure of the  $R3c$  bulk ground state, we compare the results for different bulk phases: (a) in the *cubic* phase where both the polarization and the tilts are suppressed, (b) in the centrosymmetric  $R\bar{3}c$  phase where the polarization—but not the tilts—is suppressed, (c) in the  $R3m$  phase where the tilts—but not the polarization—are suppressed, and (d) the ground state  $R3c$  phase (cf. Fig. 1). Here the structures (a)–(c) are artificial structures to isolate the structural peculiarities of the  $R3c$  phase. For each phase, we have determined the magnetic ground state and have extracted the magnetic exchange interaction beyond the first-nearest-neighbor approximation, the DM interaction, and the magnetocrystalline anisotropy. In all cases, a large exchange frustration is found, i.e., the exchange interaction of different neighbors competes in strength and sign. Despite its large frustration, the exchange interaction favors the collinear order. In both *cubic* and  $R\bar{3}c$  phase, the DM interaction is vanishing, which is why there the G-AFM is the magnetic ground state. Contrarily, both the  $R3m$  and the  $R3c$  exhibit a cycloidal ground state whose chirality is driven by a left rotating DM interaction. Counterintuitively, in the vicinity of the *R* point, the DM interaction originates from the SOC contribution of the Fe sites, with little to no contributions from the *p* orbitals of both the bismuth and

TABLE I. DFT calculated structural parameters of the  $R3c$  phase of BFO, compared with reported theoretical and experimental values.

	Bi ( $2a$ )	Fe ( $2a$ )	O ( $6b$ )	$a_{\text{th}}$ (Å)	$\alpha$ (deg)	$\Omega$ (Å <sup>3</sup> )
This work	(0,0,0)	(0.225,0.225,0.225)	(0.541,0.939,0.394)	5.54	59.71	119.32
Theory [2]	(0,0,0)	(0.227,0.227,0.227)	(0.542,0.943,0.397)	5.52	59.84	118.34
Expt. [37]	(0,0,0)	(0.221,0.221,0.221)	(0.538,0.933,0.395)	5.63	59.35	124.60

oxygen. From the comparison of the phases it is evident that the Fe-Bi displacement, responsible for the strong polarization in BFO, creates a DM interaction which stabilizes the cycloid while the octahedral tilts destabilize it: The value of the DM interaction is strongly reduced by the presence of the tilts in  $R3c$  compared to  $R3m$ .

This paper is organized as follows: Section II explains the methodologies, in particular the approach of the generalized Bloch theorem for spin spirals [6]; in Sec. III we discuss the results of the calculations carried out for the four different phases mentioned above. In Sec. IV we compare the stability of the cycloids and assess their stabilization mechanisms; A brief conclusion is given in Sec. V.

## II. METHODS

### A. Structural relaxation

The  $R3c$  unit cell of BFO containing 10 atoms is relaxed with DFT, carried out using the ABINIT package [38–40] and the projector augmented wave (PAW) method [41]. The exchange and correlation functional is treated with local spin density approximation  $+U$  (LSDA $+U$ ), with a Hubbard  $U$  parameter of 4.0 eV and  $J$  of 0.4 eV on the Fe atoms, which is typical for first-principles calculations on BFO [42,43]. The wave functions are expanded using plane-wave basis sets with a kinetic energy cutoff of 30 Hartree. The self-consistent calculations are performed with an unshifted  $24 \times 24 \times 24$   $k$ -point grid. For structural relaxation, the collinear G-type AFM configuration is adopted. The  $R3c$  structure is optimized until the force on each atom is smaller than  $1 \times 10^{-5}$  Ha/bohr. As shown in Table I, the relaxed rhombohedral lattice constant of  $R3c$ -BFO is 5.538 Å and the rhombohedral angle is  $59.71^\circ$ , in good agreement with the theoretical values in Refs. [2,43] and the experimental values of 5.63 Å and  $59.35^\circ$  [37], considering that LDA often underestimates the lattice constant by 1–2%. The relaxed atomic positions are also in good accordance with other reported values.

The  $R3m$  (resp.  $R\bar{3}c$ ) structure in this study is generated from the  $R3c$  structure by removing the  $a^-a^-a^-$  oxygen octahedral tiltings (resp. the polar displacements on Bi, Fe, and O atoms). The lattice vectors are kept unchanged. For our *cubic* structure, both the tiltings and polar displacements are removed, and the rhombohedral angle is changed to  $60^\circ$ , while keeping the lattice parameter unchanged as compared with  $R3c$ .

### B. Magnetic energy dispersion and magnetic interactions

To determine the magnetic ground state and magnetic interactions, we use the above-mentioned structures and calculate the energy dispersions  $E(\mathbf{q})$  of flat homogeneous spin spirals [6] applying the full-potential linearized augmented plane

wave (FLAPW) approach [44–46], as implemented in the FLEUR *ab initio* package [47]. For all these calculations, we have used the local density approximation [48], muffin-tin radii of 2.80 bohrs, 2.29 bohrs, and 1.29 bohrs for Bi, Fe, and O atoms, respectively, and a large plane-wave cutoff  $k_{\text{max}}$  of  $4.6 \text{ bohr}^{-1}$ . These parameters result in a magnetic moment of  $m = 4 \mu_B$  for all phases in agreement with experiments [49–51]. Spin spirals are the general solution of the Heisenberg model on a periodic lattice and can be characterized by the spin spiral vector  $\mathbf{q}$ . This vector determines the propagation direction of the spin spiral as well as the canting angle between two neighboring spins. A magnetic moment  $\mathbf{m}_i$  at an atom position  $\mathbf{r}_i$  is given by

$$\mathbf{m}_i = m(\cos(\mathbf{q} \cdot \mathbf{r}_i), \sin(\mathbf{q} \cdot \mathbf{r}_i), 0), \quad (1)$$

where  $m$  is the magnitude of the magnetic moment. The vector  $\mathbf{q}$  is a vector in reciprocal space and we choose it along the high symmetry directions of the cubic Brillouin zone (BZ, for the cubic case), R-X-M- $\Gamma$ -R and in the respective directions of the rhombohedral BZ for the rhombohedral phases. In order to compare and visualize the energy dispersions for all calculated phases, the energies are presented in the pseudocubic BZ along R-X-M- $\Gamma$ -R directions. Every point in the BZ represents a certain collinear state, e.g., the  $\Gamma$  point is the ferromagnetic (FM) state and the R point the G-type AFM state. Along the full paths, self-consistent calculations without SOC have been performed using the generalized Bloch theorem [23] with a  $k$ -point mesh of  $10 \times 10 \times 10$ . To accurately determine the energies around the magnetic ground state at  $|\mathbf{q}| \rightarrow \text{R}$ , the magnetic force theorem [52,53] has been applied using a large  $k$ -point set of 64 000 (i.e.,  $40 \times 40 \times 40$ ). The Heisenberg exchange interaction constants  $J_{ij}$  beyond first nearest neighbors of each phase are then determined by mapping the Heisenberg Hamiltonian

$$\mathcal{H} = - \sum_{ij} J_{ij}(\mathbf{m}_i \cdot \mathbf{m}_j) \quad (2)$$

onto the resulting energy dispersion  $E(\mathbf{q})$ . Here, the number of required neighbors to describe the exchange interaction is determined by finding the best overall fit of the energy dispersion, for which including more neighbors will not give a significantly better description (for detailed information, see Appendix A). As the exchange interaction appears to be frustrated (i.e., different neighbors  $J_{ij}$  compete in sign and strength to form the magnetic ground state), we also determine the exchange interaction in an effective first-nearest-neighbor approximation  $J_{\text{eff}}$ , which coincides with the so-called exchange stiffness  $A$ .  $J_{\text{eff}}$  can be interpreted as a measure of the curvature in the energy dispersion very close to the magnetic ground state, here, for  $E(\mathbf{q} \rightarrow \text{R})$ . The strength of exchange frustration can be determined in two ways, either by comparing the energy contributions of the different neighbors  $J_{ij}$  or by comparing the ratio between the effective nearest neighbor

exchange  $J_{\text{eff}}$  and the exchange interaction of the first neighbor  $J_1$ . For the latter, a ratio of  $J_{\text{eff}}/J_1 \sim 1$  is a sign of a very small exchange frustration, whereas systems with a ratio  $J_{\text{eff}}/J_1 \ll 1$  are known as highly exchange frustrated.

For each point calculated with the magnetic force theorem at  $\mathbf{q} \rightarrow \mathbf{R}$ , spin-orbit coupling is added in first-order perturbation theory [24]. The energy contribution due to SOC,  $\Delta E_{\text{SOC}}$ , is used to determine the strength of the DM interaction (the magnitude of the DM vector  $\mathbf{D}_{ij}$ ) by mapping the DM Hamiltonian

$$\mathcal{H}_{\text{DM}} = - \sum_{ij} \mathbf{D}_{ij} \cdot (\mathbf{m}_i \times \mathbf{m}_j) \quad (3)$$

to the total SOC contribution (cf. Appendix A). Here, a  $k$ -point mesh of  $20 \times 20 \times 20$  has been used.

We determine the uniaxial magnetocrystalline anisotropy energy (MAE) in the approximation of an easy axis anisotropy  $\mathbf{u}$  parallel to the  $\langle 111 \rangle$  directions according to the Hamiltonian

$$\mathcal{H}_{\text{ani}} = - \sum_i K(\mathbf{m}_i \cdot \mathbf{u})^2. \quad (4)$$

We self-consistently perform scalar-relativistic calculations in the collinear G-type AFM state and use the force theorem [52] imposing the SOC quantization axis along the  $[111]$  direction ( $E_{\parallel}$ ) and perpendicular to this direction  $[1\bar{1}0]$ , denoted as  $E_{\perp}$  (for completeness, also the  $[11\bar{2}]$  direction has been checked). The MAE is then defined as  $E_{\text{MAE}} = E_{\parallel} - E_{\perp}$ . As for the DM interaction, a  $k$ -point mesh of  $20 \times 20 \times 20$  has been applied.

### III. RESULTS

#### A. Cubic phase

In the *cubic* phase [see Fig. 1(a)], both the antiphase tilting of the O atoms and off-centering of Fe and Bi are lacking, i.e., the system is centrosymmetric, and we expect neither a DM interaction nor a polarization to be formed. This case is the simplest one and a good benchmark for our DFT calculations.

In Fig. 2(a), the energy dispersion for flat spin spiral states without spin-orbit coupling (SOC) along the high-symmetry paths of the pseudocubic Brillouin zone (BZ, see inset)  $\mathbf{R}$ - $\mathbf{X}$ - $\mathbf{M}$ - $\Gamma$ - $\mathbf{R}$  is presented. All points show the results of the energy dispersion  $E(\mathbf{q})$  obtained from DFT calculations, as a function of the different  $\mathbf{q}$  vectors. The line is the fit of  $E(\mathbf{q})$  using the Heisenberg exchange interaction (for more details, see Appendix A). In order to fit such a curve, the function needs to reproduce the energy minimum in the vicinity of the  $\mathbf{R}$  point (G-AFM) and  $\mathbf{M}$  point (in-plane checkerboard AFM) as well as the two maxima at the  $\mathbf{X}$  and the  $\Gamma$  points (FM). These maxima have a high energy of around 200 meV/atom and 370 meV/atom, respectively. This rather large energy difference is usually a sign of hard magnetic behavior and small exchange frustration, since it typically coincides with a quick increase of the energy when leaving the magnetic ground state. The nearest neighbor exchange interaction  $J_1 = -31$  meV is strongly antiferromagnetic and it prevents neighboring Fe magnetic moments from spontaneously flipping into ferromagnetic order. However, close to the  $\mathbf{R}$  point, the energy dispersion appears to be flatter than anticipated from the large  $J_1$ .

We determine the effective nearest neighbor exchange interaction of  $J_{\text{eff}} = -21$  meV to quantify this ‘‘flatness’’ in the

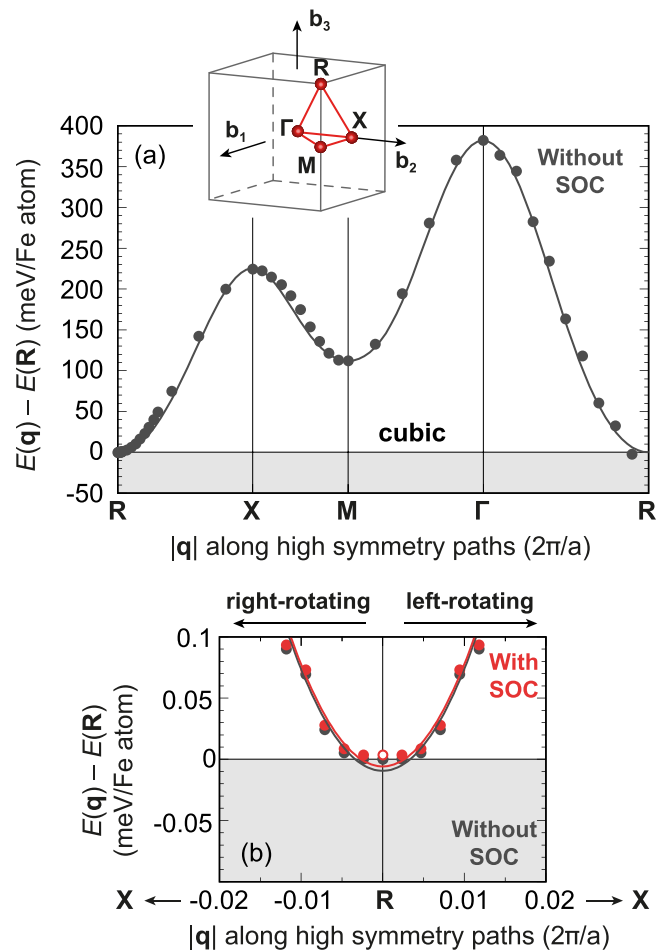


FIG. 2. Energy dispersion  $E(\mathbf{q})$  of homogeneous, flat spin spiral states for pseudocubic  $\text{BiFeO}_3$  [cf. Fig. 1(a)] with respect to the G-type AFM structure energy  $E(\mathbf{R})$ . (a) Energy dispersion without spin-orbit coupling (SOC) along the high-symmetry directions of the pseudocubic first Brillouin zone. The points are spin spiral energies computed from DFT and the lines are obtained by mapping the Heisenberg exchange Hamiltonian to the DFT data. The directions of high symmetry paths are shown in the inset. (b) Zoom around the  $\mathbf{R}$  point for left (positive) and right-rotating (negative) spin spiral states with (red) and without (gray) SOC. Note that the energy scale is below 0.1 meV. The fit including SOC (red curve) contains exchange beyond first nearest neighbors, Dzyaloshinskii-Moriya interaction and uniaxial anisotropy energy. Note that the red circle at the  $\mathbf{R}$  point is only shifted by  $K/2$  [ $K$  being the uniaxial magnetocrystalline anisotropy defined in Eq. (4)] to keep the red points continuous. In that case, the ground state is at  $E = 0$  meV/Fe atom.

energy dispersion for  $E(\mathbf{q} \rightarrow \mathbf{R})$ . The energy for very small canting angles in a spin spiral is reduced compared to the parabolic behavior for large nearest neighbor exchange  $J_1$  alone. Taking these two properties into account, the ratio of  $J_{\text{eff}}/J_1 \sim 0.68$  is a sign of large exchange frustration in the artificial *cubic* phase of BFO. Similar frustrated exchange interaction has been reported in ultrathin magnetic films [26,54–56]. Here, it occurs due to the hybridization of Fe with both oxygen and bismuth, even without structural distortion.

To fully account for this exchange frustration, seven neighbors for the exchange interaction are required to model the

TABLE II. Magnetic interactions in BiFeO<sub>3</sub> mapping an atomistic spin model to the results of DFT calculations in the conventions *per atom* and *per pair per m<sup>2</sup>*. All values of the *i*th neighbor exchange  $J_i$ , Dzyaloshinskii-Moriya constant  $D$ , and uniaxial magnetocrystalline anisotropy  $K$  are given in meV.  $J > 0$  ( $J < 0$ ) represents FM (AFM) order,  $D > 0$  ( $D < 0$ ) counterclockwise (clockwise) rotation.  $K < 0$  denotes a [111] directed easy magnetization direction and  $K > 0$  prefers an easy plane perpendicular to the [111] directions. The corresponding dispersion curves are shown in Figs. 2, 3, 4, 5. Note that the values for the DM interaction for  $R3m$  and  $R3c$  are adapted to fit the spin spiral minimum in Figs. 4(b) and 5(b). To obtain a spin spiral pitch of 62 nm in the  $R3c$  phase, the DM interaction would have to be  $D = +0.466$  meV (see Discussion).

		<i>cubic</i> phase									
	$J_1$	$J_2$	$J_3$	$J_4$	$J_5$	$J_6$	$J_7$	$J_{\text{eff}}$	$D$	$K$	
meV/atom	-31.542	-1.645	-0.657	-1.338	+0.148	+0.126	-0.075	-21.110	$\pm 0$	+0.0073	
meV/ $\mu_B^2$ /pair	-3.943	-0.206	-0.082	-0.167	+0.019	+0.016	-0.009	-2.639	$\pm 0$	+0.0005	
		$R\bar{3}c$ phase									
	$J_1$	$J_2$	$J_3$	$J_4$	$J_5$	$J_6$	$J_7$	$J_{\text{eff}}$	$D$	$K$	
meV/atom	-28.174	-1.927	-0.196	-1.216	-0.081	+0.022	-0.084	-16.156	$\pm 0$	+0.239	
meV/ $\mu_B^2$ /pair	-3.522	-0.241	-0.025	-0.152	-0.010	+0.003	-0.011	-2.020	$\pm 0$	+0.0149	
		$R3m$ phase									
	$J_1$	$J_2$	$J_3$	$J_4$	$J_5$	$J_6$	$J_7$	$J_{\text{eff}}$	$D$	$K$	
meV/atom	-33.820	-1.716	-0.026	-2.331	-	-	-	-17.758	+0.636	-0.187	
meV/ $\mu_B^2$ /pair	-4.228	-0.215	-0.003	-0.291	-	-	-	-2.220	+0.080	-0.0117	
		$R3c$ phase									
	$J_1$	$J_2$	$J_3$	$J_4$	$J_5$	$J_6$	$J_7$	$J_{\text{eff}}$	$D$	$K$	
meV/atom	-27.814	-1.475	-0.163	-0.940	-0.027	+0.069	-0.512	-11.780	+0.342	+0.069	
meV/ $\mu_B^2$ /pair	-3.477	-0.184	-0.020	-0.118	+0.003	+0.009	-0.064	-1.473	+0.043	+0.0043	

DFT calculated points of Fig. 2(a) (all determined values  $J_1, \dots, J_7$  are displayed in Table II). This procedure results in the dark gray line. The description of *cubic* BFO based on the extended Heisenberg model agrees well with the calculations: It can reproduce the maxima of energy at the X and the  $\Gamma$  point and the local energy minimum at the M point. Note that this would not be possible by solely taking  $J_1$  or  $J_{\text{eff}}$  into account. Despite the large AFM nearest neighbor exchange, the contributions of farther neighbors such as  $J_2 \sim 5\%J_1$  and  $J_4 \sim 4\%J_1$  have a significant contribution and lead to the large exchange frustration in the system.

To scrutinize the magnetic ground state, we zoom in on the energy dispersion close to  $\mathbf{q} \rightarrow R$  [Fig. 2(b)], for energy differences smaller than 0.1 meV. The G-type AFM structure represents the energy minimum without SOC (gray points and line). Due to the exchange frustration, even a small distortion triggered by internal strain might be sufficient to induce an energy minimum away from the G-type AFM state. When SOC is included (red points and curve) the magnetic ground state does not change. In fact, the DM interaction is completely suppressed (cf. Table II) as expected since the *cubic* phase is centrosymmetric, and additionally, the uniaxial anisotropy energy is extremely small. From these results, we conclude that in a hypothetical *cubic* structure of BFO, the magnetic ground state is the G-type AFM. To obtain a spin cycloidal ground state, we need to take further structural effects into account, which we describe in the following.

### B. $R\bar{3}c$ phase

Next, we explore the magnetic properties of the  $R\bar{3}c$  phase [see Fig. 1(b)], which has a lower symmetry than the *cubic*

crystal structure. In this case, the polarization is still absent so the structure has inversion symmetry but fewer mirror planes due to the presence of the oxygen octahedral tilts. This means that the oxygen along the Fe-O-Fe bonds is not a center of inversion anymore.

The energy dispersion  $E(\mathbf{q})$  without SOC in the  $R\bar{3}c$  phase is shown in Fig. 3(a). It is comparable to that in the *cubic* phase [cf. Fig. 2(a)] with only minor changes, e.g., the energy difference between R and the other points of the BZ, X, M,  $\Gamma$  are reduced and so is  $J_1 \sim -28$  meV (cf. Table II). The curvature in  $R\bar{3}c$  BFO appears flatter than in the *cubic* phase as the effective nearest neighbor exchange  $J_{\text{eff}} = -16.16$  meV/atom is reduced. Consequently, the exchange frustration is enhanced because the ratio of  $J_{\text{eff}}/J_1 = 0.57$  is slightly smaller. To fully describe the behavior of the energy dispersion, again, the exchange interaction of seven neighbors needs to be taken into account, where especially  $J_2 \sim 7\%J_1$  and  $J_4 \sim 4\%J_1$  have large contributions. Thus, comparing the *cubic* and the  $R\bar{3}c$  phase, the antiferrodistortions do not majorly affect the exchange interaction; however, small structural distortions lead to a slight change in the hybridization of the Fe orbitals with O and Bi and the exchange frustration is increased.

Due to the oxygen octahedral tilts, a DM interaction can emerge between Fe pairs mediated by the oxygen atoms, due to the lack of mirror planes [22]. However, each Fe atom is surrounded by six such pairs and serves as center of inversion. This results in the cancellation of the overall DM interaction for each Fe atom in the  $R\bar{3}c$  phase of BFO: Antiferrodistortion is not enough to destabilize the G-type AFM state and to form a spin cycloid. However, it is known that AFD tilts in  $R\bar{3}c$ -BFO can give rise to a DM interaction of a particular

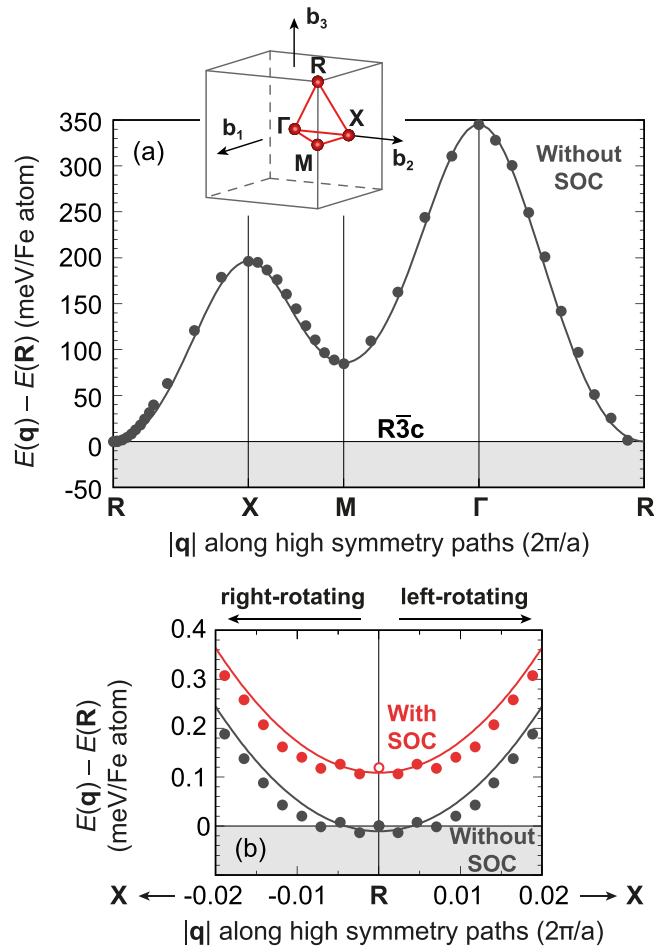


FIG. 3. Energy dispersion  $E(\mathbf{q})$  of homogeneous, flat spin spiral states for  $R\bar{3}c$   $\text{BiFeO}_3$  [cf. Fig. 1(b)] with respect to the G-type AFM structure energy  $E(\mathbf{R})$ . (a) Energy dispersion without spin-orbit coupling (SOC) along the high symmetry directions of the pseudocubic first Brillouin zone. The points and the line are spin spiral energies computed from DFT and obtained by mapping the Heisenberg exchange Hamiltonian to the DFT data, respectively. The directions of high symmetry paths are shown in the inset. (b) Zoom around the R point for left (positive) and right-rotating (negative) spin spiral states with (red) and without (gray) SOC. Note that the energy scale is below 0.4 meV. The fit including SOC (red curve) contains exchange beyond first nearest neighbors, Dzyaloshinskii-Moriya interaction and uniaxial anisotropy energy. Note that the red circle at the R point is only shifted by  $K/2$  to keep the red points continuous. In that case, the ground state is at  $E = 0$  meV/Fe atom.

symmetry that induces a noncollinear spin canting [14,15,32]; within the present approach, only flat spin spiral states are considered, and the determination of the DM interaction responsible for this spin canting is not accessible.

In the closeup of Fig. 3(b) [note that the energy range is different from Fig. 2(b) but still extremely small], the G-AFM state is the magnetic ground state, stabilized by a large easy plane (111) anisotropy of  $K = +0.24$  meV (cf. red points and curve with SOC and Table II). Therefore, compared to the *cubic* phase, the AFD not only increases the exchange frustration but also the anisotropy.

### C. $R3m$ phase

In the  $R3m$  phase [see Fig. 1(c)], both Fe and Bi atoms are displaced in the [111] direction with respect to the *cubic* phase, yielding a finite polarization. Since no AFD tilts are present, the Fe-O-Fe bonds conserve a mirror plane through the O atom and perpendicular to the bonds. This means that a DM interaction can occur only perpendicular to the Fe-O-Fe plane.

Figure 4(a) shows the energy dispersion  $E(\mathbf{q})$  without SOC for BFO in the  $R3m$  phase. As in the *cubic* and  $R\bar{3}c$  case [cf. Figs. 2 and 3(a)], the dispersion curve shows the two maxima at the X and the  $\Gamma$  point. The energy difference between the R and the  $\Gamma$  point is increased up to  $E = 400$  meV/Fe atom which explains the increased nearest-neighbor exchange interaction  $J_1 \sim -34$  meV (cf. Table II). The frustration of exchange is increased compared to the previously discussed phases with the effective nearest neighbor exchange of  $J_{\text{eff}} = -17.76$  meV/atom close to the R point and a ratio of  $J_{\text{eff}}/J_1 = 0.52$ . Along the complete high symmetry path, four shells were considered in the extended Heisenberg Hamiltonian to fit the DFT results where  $J_4 \sim 0.07 J_1$  (due to the appearance of the DFT data compared to both *cubic* and  $R\bar{3}c$  phase, including more neighbors into the model will not give a significantly better description of the energy dispersion, cf. Appendix A).

The energy dispersion curve without SOC is again very flat near the R point [gray points and curve in Fig. 4(b)]. Including SOC (red points and curve) does not stabilize the collinear G-AFM ground state as in the *cubic* or  $R\bar{3}c$  phase but an AFM spin cycloidal ground state with a pitch length of about  $\lambda \sim 63$  nm considering the energy minimum in the fit. The proximity of this value to the experimental pitch of the AFM spin cycloid present in the  $R3c$  phase is fortuitous. The propagation direction is along  $[1\bar{1}0]$  (from R  $[\frac{1}{2}, \frac{1}{2}, \frac{1}{2}]$  to X  $[1, 0, \frac{1}{2}]$ ), and the spins lie in the plane formed by the polarization in [111] and  $\mathbf{q}$  in  $[1\bar{1}0]$ , dictated by the DM interaction direction of  $[11\bar{2}]$  [Fig. 4(c)]. This ground state can arise because the ferroelectric displacement in  $R3m$  leads to a large DM interaction ( $D \sim 0.6$  meV in  $[11\bar{2}]$  direction, cf. Table II). Figure 4(c) shows the energy contribution to the energy dispersion due to the presence of spin-orbit coupling, where we observe that the contributions of both Bi (green) and O (blue) are negligible. The large DM interaction therefore stems from the change in the internal potential of the Fe atoms (red) as it also has been shown in Ref. [57]. Here, the Fe atoms contain the only net SOC contribution (black). The magnetocrystalline anisotropy ( $K = -0.19$  meV, cf. Table II) is quantitatively reduced compared to the antiferrodistorted  $R\bar{3}c$  phase, and furthermore, the preferred magnetization direction changes from an easy plane perpendicular to an easy axis collinear to the (111) directions. From these results, we conclude that the Fe-Bi ferroelectric displacements play a decisive role for BFO to exhibit a spin cycloid ground state since it introduces a nonvanishing DM interaction.

### D. $R3c$ phase

We now turn to the structure ground state of BFO, e.g., the  $R3c$  phase [see Fig. 1(d)]. This phase includes the effects of both antiferrodistortion, as in  $R\bar{3}c$ , and the ferroelectric

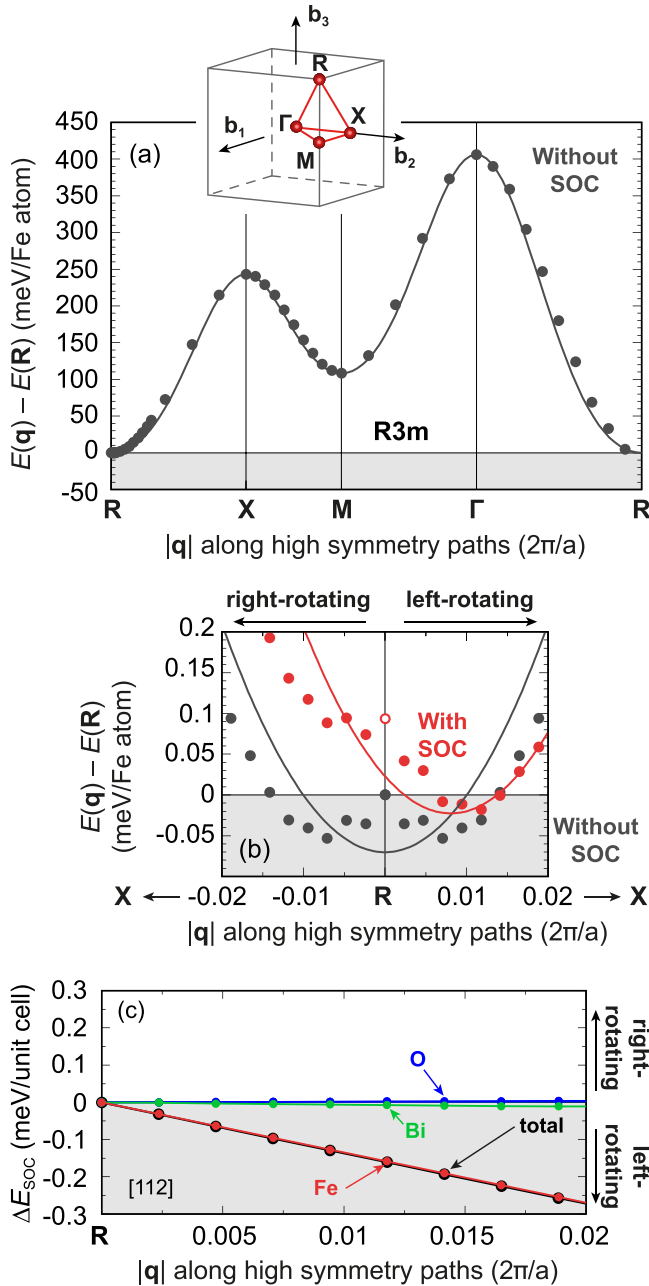


FIG. 4. Energy dispersion  $E(\mathbf{q})$  of homogeneous, flat spin spiral states for  $R3m$   $\text{BiFeO}_3$  [cf. Fig. 1(c)] with respect to the G-type AFM structure energy  $E(\mathbf{R})$ . (a) Energy dispersion without spin-orbit coupling (SOC) along the high symmetry directions of the pseudocubic first Brillouin zone. The points and the line are spin spiral energies computed from DFT and obtained by mapping the Heisenberg exchange Hamiltonian to the DFT data, respectively. The directions of high symmetry paths are shown in the inset. (b) Zoom around the R point for left (positive) and right-rotating (negative) spin spiral states with (red) and without (gray) SOC. Note that the energy scale is below 0.2 meV. The fit including SOC (red curve) contains exchange beyond first nearest neighbors, Dzyaloshinskii-Moriya interaction and uniaxial anisotropy energy. Due to slight deviations stemming from the exchange interaction, the value for the DM interaction has been adapted to better describe the energy dispersion with SOC. Note that the red circle at the R point is only shifted by  $K/2$ . (c) Element-resolved energy contribution due to spin-orbit coupling  $\Delta E_{\text{SOC}}$  to the energy dispersion of spin spirals calculated in the  $[11\bar{2}]$

displacements of the  $R3m$  phase. The energy dispersion without SOC [Fig. 5(a)] looks similar to all previously discussed phases, consequently, the exchange interaction (cf. Table II) is also strongly frustrated. The energy differences along the whole high symmetry path are the smallest of all phases and  $J_1 = -28$  meV/atom. Note that in BFO in general, the antiferromagnetic exchange interaction is large and prevents the system from spontaneously changing the magnetic order. While  $J_1$  is still comparable with the other calculated phases, due to the very flat energy dispersion at  $\mathbf{q} \rightarrow \mathbf{R}$ ,  $J_{\text{eff}} = -11.8$  meV/atom is by far the smallest. Consequently, the magnetic exchange frustration is maximized in the  $R3c$  phase with a ratio of  $J_{\text{eff}}/J_1 = 0.42$ . To capture these effects, seven neighbors are included to describe  $E(\mathbf{q})$  along the whole path. Here, especially  $J_4 \sim 0.035 J_1$  and  $J_7 = 0.018 J_1$  contribute strongly to the exchange frustration.

In this phase, it is actually possible to measure the exchange interaction via inelastic neutron scattering [51,58]. The reported values of  $J_1$  are  $\sim 4.4$  meV/pair (values given per pair obtained for  $m_i = 5 \mu_B$  in Ref. [58]) and  $m_i \sim 4 \mu_B$  (values are given per atom at 5 K in Ref. [51]) in very good agreement with  $J_1 = 3.5$  meV/pair (obtained for  $m_i = 4 \mu_B$  in our case) in this work. The difference between these two measures can be explained by the different number of shells used on this work.

Despite the large exchange frustration, a G-AFM state is expected when SOC is neglected [dark gray curve without SOC in Fig. 5(b)]. Including SOC and the two previously separated effects of the  $R\bar{3}c$  and  $R3m$  phases, the magnetic ground state in the  $R3c$  phase changes to an AFM spin cycloid with a pitch length of about 80 nm [red points in Fig. 5(b)]. This is in good agreement with the experimentally measured value of 62 nm in bulk BFO [7,8] and the theoretical value of 83 nm [22]. The propagation direction of the cycloid is along  $[1\bar{1}0]$  with the spins perpendicular to the DM interaction direction of  $[11\bar{2}]$ . [Note that only in  $[11\bar{2}]$  the DM interaction is nonzero, cf. Fig. 5(c)].

Compared to the  $R3m$  phase, the DM interaction in  $R3c$  BFO is reduced ( $D \sim 0.34$  meV, cf. Table II), but the whole contribution of SOC still stems from the Fe atoms [red points in Fig. 5(c)], and the calculated DMI energy of 0.04 meV at  $q = 0.0065(2\pi/a)$ , where the total energy is minimized, agrees reasonably with the reported experimental value of 0.07 meV [59]. Since both structural perturbations are present in the  $R3c$  phase, the DM interaction and MAE are smaller compared to the phases showing only one of these perturbations (cf. Table II). The smaller DM interaction with respect to the  $R3m$  phase can be explained by the inclusion of the  $R\bar{3}c$  structure with vanishing DM interaction into  $R3c$  BFO, effectively reducing its magnitude. In a similar way, the anisotropy of the  $R3c$  phase can be seen as a sum of two structural effects and their opposing anisotropy contributions, leading to the reduced anisotropy of  $K \sim +0.07$  meV. The reported value of

direction. Shown are the total (black), Fe (red), Bi (green), and O (blue) contributions. Due to an antiferromagnetic unit cell, each atom appears twice with the same contribution. Here, the lines serve as a guide to the eye.

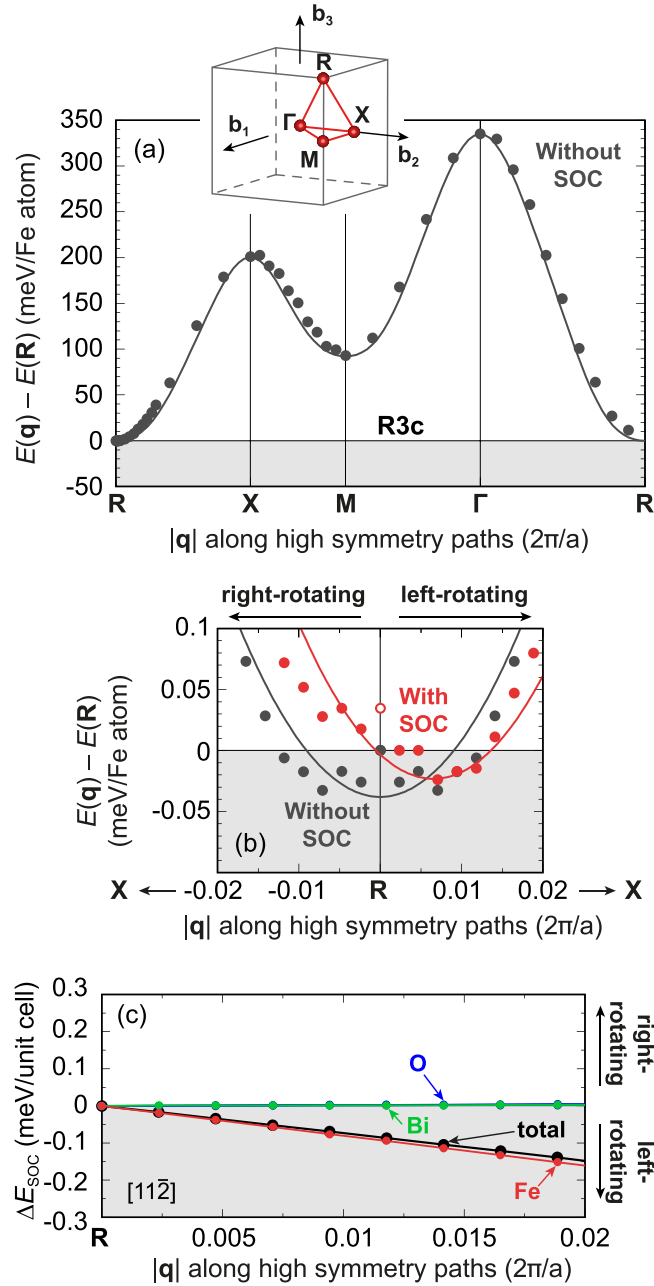


FIG. 5. Energy dispersion  $E(\mathbf{q})$  of homogeneous, flat spin spiral states for  $R3c$   $\text{BiFeO}_3$  [cf. Fig. 1(d)] with respect to the G-type AFM structure energy  $E(\mathbf{R})$ . (a) Energy dispersion without spin-orbit coupling (SOC) along the high symmetry directions of the pseudocubic first Brillouin zone. The points and the line are spin spiral energies computed from DFT and obtained by mapping the Heisenberg exchange Hamiltonian to the DFT data, respectively. The directions of high symmetry paths are shown in the inset. (b) Zoom around the R point for left (positive) and right-rotating (negative) spin spiral states with (red) and without (grey) SOC. Note that the energy scale is below 0.1 meV. The fit including SOC (red curve) contains exchange beyond first nearest neighbors, Dzyaloshinskii-Moriya interaction and uniaxial anisotropy energy. Due to slight deviations stemming from the exchange interaction, the value for the DM interaction has been adapted to better describe the energy dispersion with SOC. Note that the red circle at the R point is only shifted by  $K/2$ . (c) Element resolved contribution due to spin-orbit coupling  $\Delta E_{\text{SOC}}$  to the energy dispersion of spin spirals calculated in the  $[11\bar{2}]$  direction. Shown are

both the DM interaction  $D = 0.107$  meV and the anisotropy  $K = 0.009$  meV in Ref. [58] are larger than our values  $D = 0.043$  meV and  $K = 0.0043$  meV, respectively, because the exchange frustration is taken into our model Hamiltonian.

#### IV. DISCUSSION

We now set the results in an experimental context and compare the different phases with each other, to understand the driving mechanisms that form the magnetic ground state in  $R3c$  BFO. For all four investigated phases, *cubic*,  $R\bar{3}c$ ,  $R3m$ , and  $R3c$ , we observe a flat energy dispersion around the energy minimum at the R point of the pseudocubic BZ [cf. Figs. 2, 3, 4, 5(b)]. This behavior can be explained by a large exchange frustration stemming from the hybridization among the three elements Bi, Fe, and O. A distortion of the perfect pseudocubic structure will not have a large effect on the exchange interaction, but slightly increase the frustration. In the  $R3c$  phase, the frustration of exchange is stronger since  $J_1$  is smaller and for instance  $J_7$  is larger in comparison with the other phases. Note that despite the large frustration, the exchange interaction will still favor the G-type AFM state because the magnetic ground state is extremely close to the collinear state.

Within our model, a spin cycloid ground state with the calculated periodicity can only be obtained by a large DM interaction. However, in the *cubic* and  $R\bar{3}c$  phases the DM interaction is zero [60]. It solely can arise due to the Fe-Bi displacement in the  $R3m$  phase (cf. Fig. 4). That means the DM interaction presented in  $R3c$  BFO originates from the ferroelectric displacement, which is also responsible for the strong polarization in BFO. This finding is in good agreement with the so-called inverse spin current model [10,12].

In total, the DM interaction competes with both exchange and anisotropy to stabilize an AFM spin cycloid in  $R3c$  BFO. A large anisotropy as calculated for either the  $R\bar{3}c$  or  $R3m$  phase would, however, stabilize the collinear order and prevent the formation of a cycloid in the  $R3c$  phase. Since the anisotropies for  $R\bar{3}c$  and  $R3m$  BFO prefer magnetization directions perpendicular to each other, the total anisotropy is reduced when both structural displacements are included into  $R3c$  BFO (cf. Table II).

Our cycloid pitch length of  $\sim 80$  nm calculated from DFT for  $R3c$  BFO agrees reasonably well with the experimentally measured one of 62 nm [7,8]. We note that in standard implementations of spin dynamics, the anisotropy energy contribution is modified for exactly collinear states. In this case for  $q$  at the R point there will be a jump in energy by  $K/2$ , which yields an energy 10  $\mu\text{eV}$  lower than the spin cycloid ground state. This is an artifact, but will not happen in full calculations, as any departure from collinearity will restore the continuous red curve energies from Fig. 5(b).

To be in perfect agreement with experimental observations, a slight decrease in the AFM spin cycloid pitch length is

← the total (black), Fe (red), Bi (green) and O (blue) contributions. Due to an antiferromagnetic unit cell, each atom appears twice with the same contribution. Here, the lines serve as a guide to the eye.



needed. This requires an enhancement of the DM interaction. In fact, to recover a magnetic ground state cycloid with 62 nm pitch—assuming the given values for the exchange interaction and anisotropy of Table II—the DM interaction would have to be  $D = 0.466 \text{ meV} = 0.059 \text{ meV}/\mu_B^2/\text{pair}$ . This value is consistent with previously reported DM interactions of  $0.18 \text{ meV}/\text{pair}$  estimated from the experimental wavelength [16,30,51], and  $0.102 \text{ meV}/\text{pair}$  calculated by density function theory using the four-state method [22].

## V. CONCLUSION

In conclusion, we applied DFT calculations to investigate the magnetic ground state of multiferroic BiFeO<sub>3</sub>. We find an AFM spin cycloid with a pitch length of  $\sim 80 \text{ nm}$  in the  $R3c$  phase which is in good agreement with experimental and previous theoretical observations. To explain the magnetic structure, we compare several artificial bulk phases with intermediate symmetry, which isolate the structural properties of the  $R3c$  bulk phase of BiFeO<sub>3</sub>: pseudocubic,  $R\bar{3}c$ , and  $R3m$ . We find that all phases show a large exchange frustration which leads to small energies required to cant the spins out of the collinear G-type AFM order. In the  $R\bar{3}c$  phase, the octahedral antiferrodistortion stabilizes the G-type AFM state due to a large anisotropy and zero net Dzyaloshinskii-Moriya interaction. The  $R3m$  phase shows ferroelectric displacements of Fe and Bi which is responsible for a strong polarization in BFO, but also for the appearance of a net DM interaction which is strong enough to destabilize the collinear order of the G-type AFM in  $R3m$  BiFeO<sub>3</sub>. The anisotropy of the  $R3m$  phase favors a magnetization direction perpendicular to that one of the  $R\bar{3}c$  phase, and the two distortions compete. Summing up all effects in the  $R3c$  phase, exchange frustration, DM interaction from the ferroelectric displacement, and the competition of both anisotropy contributions from  $R3m$  and  $R\bar{3}c$  lead to the stabilization of an AFM spin cycloid in BiFeO<sub>3</sub> with a long cycloid period.

## ACKNOWLEDGMENTS

This work is supported by the National Natural Science Foundation of China under Grant No. 12074277, Natural Science Foundation of Jiangsu Province (BK20201404), the startup fund from Soochow University and the support from Priority Academic Program Development (PAPD) of Jiangsu Higher Education Institutions. S.M., M.J.V., B.D., and L.B. acknowledge the DARPA Grant No. HR0011727183-D18AP00010 (TEE Program). L.B. also thanks ARO Grant No. W911NF-21-1-0113. M.J.V. acknowledges funding by the Belgian FNRS (PDR G.A. T.1077.15, T.0103.19, and an “out” sabbatical grant to ICN2 Barcelona), and the Communauté Française de Belgique (ARC AIMED G.A. 15/19-09). This work used the ARCHER2 UK National Supercomputing Service [61] and further computational resources have been provided by the Blue Waters sustained-petascale computing project at the National Center for Supercomputing Applications (NCSA).

## APPENDIX A: DESCRIPTION OF HEISENBERG EXCHANGE AND DM INTERACTIONS IN THE PSEUDOCUBIC LATTICE

In the main text, we map the energy dispersions without spin-orbit coupling (SOC) onto the Heisenberg exchange interaction beyond first nearest neighbors to determine the strength of the exchange constants  $J_{ij}$ . To understand the procedure of mapping and the applied formulas, we provide an example for the nearest neighbor along the R-X direction of the cubic Brillouin zone (BZ). The Heisenberg exchange interaction between two (normalized) magnetic moments  $\mathbf{m}_i$ ,  $\mathbf{m}_j$  at positions  $\mathbf{R}_i$ ,  $\mathbf{R}_j$  is described via

$$\mathcal{H} = - \sum_{ij} J_{ij} (\mathbf{m}_i \cdot \mathbf{m}_j). \quad (\text{A1})$$

The general solutions of the Heisenberg model on a discrete lattice are homogeneous flat spin spirals characterized by the spin spiral vector  $\mathbf{q}$ . We perform first principles calculations of these spirals to constrain and fit the model. Transferring Eq. (A1) into reciprocal space leads to

$$\mathcal{H} = -N \sum_{\mathbf{q}} J(\mathbf{q}) \mathbf{m}_{\mathbf{q}} \cdot \mathbf{m}_{\mathbf{q}}, \quad (\text{A2})$$

where  $N$  is the number of interacting magnetic moments and the exchange constant

$$\begin{aligned} J(\mathbf{q}) &= \sum_{\delta} J_{0\delta} e^{-i\mathbf{q} \cdot \mathbf{R}_{\delta}} \\ &= \sum_{\delta} J_{0\delta} (\cos(\mathbf{q} \cdot \mathbf{R}_{\delta}) - i \sin(\mathbf{q} \cdot \mathbf{R}_{\delta})). \end{aligned} \quad (\text{A3})$$

The parameter  $\delta$  denotes the respective neighboring distance in real space. The resulting energy contribution then is

$$E = -N S^2 J(\mathbf{q}). \quad (\text{A4})$$

The spin spiral vector  $\mathbf{q}$  can be defined as

$$\mathbf{q} = q_1 \mathbf{b}_1 + q_2 \mathbf{b}_2 + q_3 \mathbf{b}_3, \quad (\text{A5})$$

where  $\mathbf{b}_1$ ,  $\mathbf{b}_2$ ,  $\mathbf{b}_3$  are the reciprocal lattice vectors. We now adapt the general formulas for the simple cubic (sc) lattice. For the sc lattice, the primitive unit vectors are given in cartesian coordinates as

$$\mathbf{a}_1 = a \begin{pmatrix} 1 \\ 0 \\ 0 \end{pmatrix}, \quad \mathbf{a}_2 = a \begin{pmatrix} 0 \\ 1 \\ 0 \end{pmatrix}, \quad \mathbf{a}_3 = a \begin{pmatrix} 0 \\ 0 \\ 1 \end{pmatrix}, \quad (\text{A6})$$

where  $a$  denotes the lattice constant and for the reciprocal lattice,

$$\mathbf{b}_1 = \frac{2\pi}{a} \begin{pmatrix} 1 \\ 0 \\ 0 \end{pmatrix}, \quad \mathbf{b}_2 = \frac{2\pi}{a} \begin{pmatrix} 0 \\ 1 \\ 0 \end{pmatrix}, \quad \mathbf{b}_3 = \frac{2\pi}{a} \begin{pmatrix} 0 \\ 0 \\ 1 \end{pmatrix}. \quad (\text{A7})$$

The respective BZ of the sc lattice is also cubic [shown in Fig. 6(a) in the inset] and has the distinct high symmetry and corner/face points  $\Gamma$ , X, M, R, which are given in internal coordinates with  $(u, v, w)$  where the reciprocal vector  $\mathbf{k}$  is

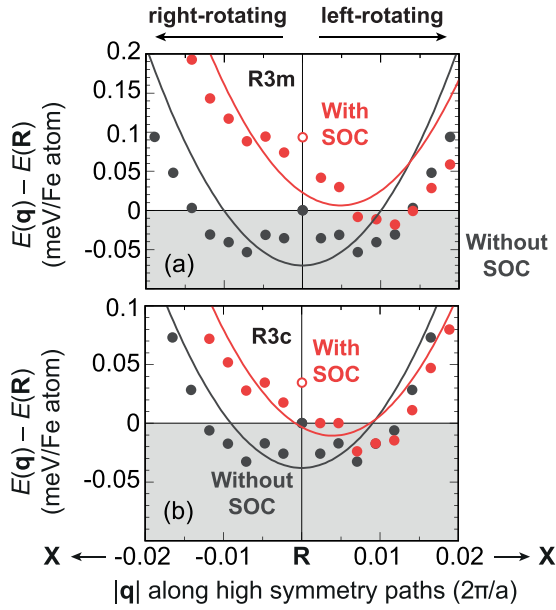


FIG. 6. Energy dispersions of homogeneous flat spin spiral states without (gray) and with (red) spin-orbit coupling (SOC) for BiFeO<sub>3</sub> (BFO) at  $|\mathbf{q}| \rightarrow \mathbf{R}$  of the pseudocubic Brillouin zone. The points show the DFT calculated energies (dark gray without SOC, red with SOC) whereas lines represent the fit to the extended Heisenberg model including the exchange interaction beyond first nearest neighbors (without SOC, gray lines), the Dzyaloshinskii-Moriya interaction and magnetocrystalline anisotropy energy (with SOC, red lines). For positive (negative) values of  $\mathbf{q}$ , the AFM spin spirals prefer a counterclockwise (clockwise) rotation. (a) *R3m* phase and (b) *R3c* phase. Note that here, all lines are based on the complete fitting of the DFT data.

defined as  $\mathbf{k} = u\mathbf{b}_1 + v\mathbf{b}_2 + w\mathbf{b}_3$ .

$$\Gamma = \begin{pmatrix} 0 \\ 0 \\ 0 \end{pmatrix}, \quad X = \begin{pmatrix} 0 \\ 1/2 \\ 0 \end{pmatrix}, \quad M = \begin{pmatrix} 1/2 \\ 1/2 \\ 0 \end{pmatrix}, \quad R = \begin{pmatrix} 1/2 \\ 1/2 \\ 1/2 \end{pmatrix}.$$

For the nearest neighbor in the sc, the scalar product of  $\mathbf{q} \cdot \mathbf{R}$  is defined as in Table III.

Inserting  $\mathbf{q} \cdot \mathbf{R}$  into Eq. (A3), the fitting formula for the nearest neighbor reads as

$$E_1 = -2J_1 \{ \cos(2\pi q_1) + \cos(2\pi q_2) + \cos(2\pi q_3) \}. \quad (\text{A8})$$

In the R-X direction, the  $\mathbf{q}$  vector goes along  $(1/2, 1/2, 1/2) \rightarrow (1, 0, 1/2)$ , which means the applied  $\mathbf{q}$  vector is  $\mathbf{q}' =$

TABLE III. Position  $\mathbf{R}$  of the nearest neighbor in Cartesian coordinates and the respective scalar product of  $\mathbf{q} \cdot \mathbf{R}$ .

Position $\mathbf{R}$	$\mathbf{q} \cdot \mathbf{R}$
$a(1, 0, 0)$	$2\pi q_1$
$a(0, 1, 0)$	$2\pi q_2$
$a(0, 0, 1)$	$2\pi q_3$
$a(-1, 0, 0)$	$-2\pi q_1$
$a(0, -1, 0)$	$-2\pi q_2$
$a(0, 0, -1)$	$-2\pi q_3$

$(1/2 - q, 1/2 + q, 1/2)$ . The length of the R-X path is  $\frac{\sqrt{2}}{2}$  and including the vector in Eq. (A8) leads to

$$\begin{aligned} E_1^{RX} &= -2J_1 \{ \cos(2\pi(1/2 - q)) \\ &\quad + \cos(2\pi(1/2 + q)) + \cos(\pi) \} \\ &= -2J_1 \{ -2 \cos(2\pi q) - 1 \} \end{aligned}$$

considering the length  
of the path

$$E_1^{RX} = -2J_1 \{ -2 \cos(\sqrt{2}\pi q) - 1 \}. \quad (\text{A9})$$

According to this procedure, we determine the formulas for mapping the exchange interaction onto the calculated values for the whole path of  $\mathbf{q}$ , R-X-M- $\Gamma$ -R.

For the DM interaction, we only focus on the magnetic ground state at the region of  $|\mathbf{q}| \rightarrow \mathbf{R}$ . The DM interaction acting on two magnetic moments  $\mathbf{m}_i$ ,  $\mathbf{m}_j$  is described with

$$\mathcal{H}_{\text{DM}} = - \sum_{ij} \mathbf{D}_{ij} \cdot (\mathbf{m}_i \times \mathbf{m}_j). \quad (\text{A10})$$

The cross product is linked to a sin behavior where a linear contribution remains close to the R point where  $q \rightarrow 0$ .

The resulting formula for the DM interaction is derived similarly as the exchange. In the R-X direction, we applied the formula for the nearest neighbor DM interaction as

$$E_{\text{DM},1}^{RX} = -4\sqrt{2}\pi D_1 q. \quad (\text{A11})$$

## APPENDIX B: DETERMINATION OF EXCHANGE AND DZYALOSHINSKII-MORIYA INTERACTION FROM FIRST PRINCIPLES

Using the description of Appendix A, we first map the exchange interaction of Eq. (A8) onto the results from the DFT calculations without spin-orbit coupling. The data are seen in the energy dispersions (cf. Fig. 6 and Fig. 1, . . . , 4 in the main text) as dark gray points and the result of the mapping is seen as dark gray lines. As energy reference for the mapping, we choose the  $\Gamma$  point in contrast to the DFT calculated values which show the R point as energy reference. We do this to not restrict the fit to go directly through the R point because around R, we reached the limit of DFT accuracy. Two main features occur to be important as a result: the overall appearance and representation of the fit for all data points along R-X-M- $\Gamma$ -R and a good representation of the DFT calculated values at the energy minimum. Here, three main problems can be seen:

(1) The larger the described spin spiral period (a small value of  $|\mathbf{q}|$  in reciprocal space), the more distant neighbors need to be taken into account (in real space) to capture these features. Here, the energy dispersion at the ground state energy is very close to the collinear state—closer than in every other system known in the literature.

(2) The energy minimum is in the range of  $\approx 50 \mu\text{eV}$ .

(3) The energy differences between the high symmetry points of the BZ—R, X, M,  $\Gamma$ —are large.

These three features are hard to accommodate and describe within a reasonable amount of interacting neighbors for the exchange interaction. Therefore, we restrict ourselves

in finding reasonable values for the exchange interaction to obtain the most reasonable agreement between the DFT calculated values and the fit. All resulting values are presented in Table II. Here, the number of included neighbors in the fit of the exchange interaction are chosen, so that including more neighbors will not give a significant improvement of the description. This criterion needs to be subjective because the points show some irregular shape due to the limit of accuracy which we reach in DFT calculations, visible in the extremely small energy windows of panels (b) of Figs. 2, 3, 4, and 5. For the two latter, e.g., we decide the best line to lie in between the first few points from R. In the case of the  $R3m$  phase, this can be achieved by including up to four neighbors and in the case of the  $R3c$  phase (due to the slightly different shape of the dispersion), seven neighbors are needed. Note that especially  $J_4, J_7$  can be seen as responsible to flatten the curve along the high symmetry directions. On the other hand,  $J_5, J_6, J_8, \dots$  will change the energy differences between the high symmetry points, which we do not desire, once the good differences are obtained. In the case of the  $R3m$  phase, the energy contributions of  $J_5, J_6, \dots$  therefore are negligible and for  $R3c$ , it is  $J_8, J_9, \dots$ . Due to slight deviations stemming from the exchange interaction in Figs. 4 and 5, the values for the DM interaction have been adapted to better describe the energy dispersion with SOC [red curve in the respective panel (b)].

The values for the DM interaction solely from DFT are obtained by mapping Eq. (A11) to the DFT results of panels (c) in Figs. 4 and 5. For these values, the curves are presented in Fig. 6. For the  $R3m$  phase, it is  $D = +0.383$  meV/atom and for the  $R3c$  phase, it is  $D = +0.207$  meV/atom. Note that

this value is still in good agreement with previously reported values.

### APPENDIX C: SENSITIVITY OF THE SPIN SPIRAL PERIOD

In the present work, the determined period of the AFM spin spiral in  $R3c$  BFO  $\lambda \sim 80$  nm from DFT calculations is in good agreement with the experimentally reported value of 62 nm [7,8]. Despite the high accuracy of the calculations, the spin spiral period  $\lambda$  is a very sensitive value since it reflects the reciprocal value of the spin spiral vector  $\mathbf{q}$ . Note that at the R point of the pseudocubic Brillouin zone,  $q \rightarrow 0$  means  $\lambda \rightarrow \infty$ . In panels (b) of Figs. 2, 3, 4, and 5, the range of  $|q| \in [0, 0.02]$  in units of  $2\pi/a$  corresponds to  $\lambda \in [\infty, 27.69$  nm]. Here, the rhombohedral lattice constant  $a = 5.538$  Å has been taken into account. As a consequence, a very small change at the energy minimum of  $q = 0.0085 \pm 0.001$   $2\pi/a$  will affect the spin spiral period approximately as  $\lambda \sim 65 \pm 8$  nm. In other words, a slight change in either exchange, DM interaction, or anisotropy has a rather large change in the respective spin spiral period. Taking the DM interaction,  $D = 0.342$  meV/atom determined from panels (b) in Fig. 5 in the main text (cf. Table II) yields a spin spiral period of  $\lambda \sim 80$  nm, while the value  $D = 0.466$  meV/atom can reproduce the experimentally observed period of  $\lambda = 62$  nm. Although the difference in  $\Delta\lambda \sim 20$  nm appears rather large, both values for the DM interaction are in very good agreement with previous reports. Even though the actual spin spiral period is such a sensitive quantity, our conclusions and the driving mechanisms are robust and will not change.

- 
- [1] Y. E. Roginskaya, Y. Y. Tomashpol'Skii, Y. N. Venevtsev, V. M. Petrov, and G. S. Zhdanov, *Sov. Phys. JETP* **23**, 47 (1966).
- [2] J. B. Neaton, C. Ederer, U. V. Waghmare, N. A. Spaldin, and K. M. Rabe, *Phys. Rev. B* **71**, 014113 (2005).
- [3] A. Glazer, *Acta Crystallogr., Sect. B: Struct. Crystallogr. Cryst. Chem.* **28**, 3384 (1972).
- [4] I. Dzyaloshinsky, *J. Phys. Chem. Solids* **4**, 241 (1958).
- [5] T. Moriya, *Phys. Rev.* **120**, 91 (1960).
- [6] Note that spin cycloids are special cases of spin spiral states when spin-orbit coupling is included. The term ‘‘cycloid’’ typically is used to describe the magnetic ground state of BFO. However, neglecting spin-orbit coupling, the spin spirals are not restricted to be cycloidal. In this paper we will use the term cycloid discussing the magnetic ground state of BFO, whereas spin spirals are used methodologically.
- [7] I. Sosnowska, T. P. Neumaier, and E. Steichele, *J. Phys. C: Solid State Phys.* **15**, 4835 (1982).
- [8] I. Sosnowska, M. Loewenhaupt, W. David, and R. Ibberson, *Phys. B: Condens. Matter* **180-181**, 117 (1992).
- [9] A. Fert and P. M. Levy, *Phys. Rev. Lett.* **44**, 1538 (1980).
- [10] H. Katsura, N. Nagaosa, and A. V. Balatsky, *Phys. Rev. Lett.* **95**, 057205 (2005).
- [11] R. de Sousa, M. Allen, and M. Cazayous, *Phys. Rev. Lett.* **110**, 267202 (2013).
- [12] A. Raeliarijaona, S. Singh, H. Fu, and L. Bellaiche, *Phys. Rev. Lett.* **110**, 137205 (2013).
- [13] B. Xu, B. Dupé, C. Xu, H. Xiang, and L. Bellaiche, *Phys. Rev. B* **98**, 184420 (2018).
- [14] C. Ederer and N. A. Spaldin, *Phys. Rev. B* **71**, 060401(R) (2005).
- [15] L. Bellaiche, Z. Gui, and I. A. Kornev, *J. Phys.: Condens. Matter* **24**, 312201 (2012).
- [16] R. S. Fishman, *Phys. B: Condens. Matter* **536**, 115 (2018).
- [17] R. de Sousa and J. E. Moore, *Phys. Rev. B* **77**, 012406 (2008).
- [18] M. Cazayous, Y. Gallais, A. Sacuto, R. de Sousa, D. Lebeugle, and D. Colson, *Phys. Rev. Lett.* **101**, 037601 (2008).
- [19] P. Rovillain, R. De Sousa, Y. Gallais, A. Sacuto, M. Méasson, D. Colson, A. Forget, M. Bibes, A. Barthélémy, and M. Cazayous, *Nat. Mater.* **9**, 975 (2010).
- [20] D. Sando, A. Agbelele, D. Rahmedov, J. Liu, P. Rovillain, C. Toulouse, I. C. Infante, A. P. Pyatakov, S. Fusil, E. Jacquet, C. Carrétéro, C. Deranlot, S. Lisenkov, D. Wang, J.-M. Le Breton, M. Cazayous, A. Sacuto, J. Juraszek, A. K. Zvezdin, L. Bellaiche, B. Dkhil, A. Barthélémy, and M. Bibes, *Nat. Mater.* **12**, 641 (2013).
- [21] I. Gross, W. Akhtar, V. Garcia, L. J. Martínez, S. Chouaieb, K. Garcia, C. Carrétéro, A. Barthélémy, P. Appel, P. Maletinsky, J.-V. Kim, J. Y. Chauleau, N. Jaouen, M. Viret,

- M. Bibes, S. Fusil, and V. Jacques, *Nature (London)* **549**, 252 (2017).
- [22] C. Xu, B. Xu, B. Dupé, and L. Bellaïche, *Phys. Rev. B* **99**, 104420 (2019).
- [23] L. M. Sandratskii, *J. Phys.: Condens. Matter* **3**, 8565 (1991).
- [24] M. Heide, G. Bihlmayer, and S. Blügel, *Phys. B: Condens. Matter* **404**, 2678 (2009).
- [25] S. Heinze, K. Von Bergmann, M. Menzel, J. Brede, A. Kubetzka, R. Wiesendanger, G. Bihlmayer, and S. Blügel, *Nat. Phys.* **7**, 713 (2011).
- [26] B. Dupé, M. Hoffmann, C. Paillard, and S. Heinze, *Nat. Commun.* **5**, 4030 (2014).
- [27] M. Hervé, B. Dupé, R. Lopes, M. Böttcher, M. D. Martins, T. Balashov, L. Gerhard, J. Sinova, and W. Wulfhekkel, *Nat. Commun.* **9**, 1015 (2018).
- [28] H. Yang, G. Chen, A. A. C. Cotta, A. T. N'Diaye, S. A. Nikolaev, E. A. Soares, W. A. A. Macedo, K. Liu, A. K. Schmid, A. Fert, and M. Chshiev, *Nat. Mater.* **17**, 605 (2018).
- [29] A. Belabbes, G. Bihlmayer, S. Blügel, and A. Manchon, *Sci. Rep.* **6**, 24634 (2016).
- [30] I. Sosnowska and A. K. Zvezdin, *J. Magn. Magn. Mater.* **140**, 167 (1995).
- [31] M. Ramazanoglu, M. Laver, W. Ratcliff, S. M. Watson, W. C. Chen, A. Jackson, K. Kothapalli, S. Lee, S.-W. Cheong, and V. Kiryukhin, *Phys. Rev. Lett.* **107**, 207206 (2011).
- [32] D. Albrecht, S. Lisenkov, W. Ren, D. Rahmedov, I. A. Kornev, and L. Bellaïche, *Phys. Rev. B* **81**, 140401(R) (2010).
- [33] Y. F. Popov, A. K. Zvezdin, G. P. Vorobév, A. M. Kadomtseva, V. A. Murashev, D. N. Rakov, and G. P. Vorob'ev, *JETP Lett.* **57**, 69 (1993).
- [34] J. Varignon, M. N. Grisolia, J. Íñiguez, A. Barthélémy, and M. Bibes, *npj Quantum Mater.* **2**, 21 (2017).
- [35] A. Manchon, H. C. Koo, J. Nitta, S. M. Frolov, and R. A. Duine, *Nat. Mater.* **14**, 871 (2015).
- [36] A. Haykal, J. Fischer, W. Akhtar, J.-Y. Chauléau, D. Sando, A. Finco, F. Godel, Y. A. Birkhölzer, C. Carrétéro, N. Jaouen, M. Bibes, M. Viret, S. Fusil, V. Jacques, and V. Garcia, *Nat. Commun.* **11**, 1704 (2020).
- [37] F. Kubel and H. Schmid, *Acta Crystallogr. Sect. B: Struct. Sci.* **46**, 698 (1990).
- [38] X. Gonze, B. Amadon, P. M. Anglade, J. M. Beuken, F. Bottin, P. Boulanger, F. Bruneval, D. Caliste, R. Caracas, M. Côté *et al.*, *Comput. Phys. Commun.* **180**, 2582 (2009).
- [39] X. Gonze, F. Jollet, F. A. Araujo, D. Adams, B. Amadon, T. Applencourt, C. Audouze, J.-M. Beuken, J. Bieder, A. Bokhanchuk *et al.*, *Comput. Phys. Commun.* **205**, 106 (2016).
- [40] X. Gonze, B. Amadon, G. Antonius, F. Arnardi, L. Baguet, J.-M. Beuken, J. Bieder, F. Bottin, J. Bouchet, E. Bousquet, N. Brouwer, F. Bruneval, G. Brunin, T. Cavignac, J.-B. Charraud, W. Chen, M. Côté, S. Cottenier, J. Denier, G. Geneste, P. Ghosez, M. Giantomassi, Y. Gillet, O. Gingras, D. R. Hamann, G. Hautier, X. He, N. Helbig, N. Holzwarth, Y. Jia, F. Jollet, W. Lafargue-Dit-Hauret, K. Lejaeghere, M. A. Marques, A. Martin, C. Martins, H. P. Miranda, F. Naccarato, K. Persson, G. Petretto, V. Planes, Y. Pouillon, S. Prokhorenko, F. Ricci, G.-M. Rignanese, A. H. Romero, M. M. Schmitt, M. Torrent, M. J. van Setten, B. Van Troeye, M. J. Verstraete, G. Zérah, and J. W. Zwanziger, *Comput. Phys. Commun.* **248**, 107042 (2020).
- [41] P. E. Blöchl, *Phys. Rev. B* **50**, 17953 (1994).
- [42] I. A. Kornev, S. Lisenkov, R. Haumont, B. Dkhil, and L. Bellaïche, *Phys. Rev. Lett.* **99**, 227602 (2007).
- [43] C. Paillard, B. Xu, B. Dkhil, G. Geneste, and L. Bellaïche, *Phys. Rev. Lett.* **116**, 247401 (2016).
- [44] H. Krakauer, M. Posternak, and A. J. Freeman, *Phys. Rev. B* **19**, 1706 (1979).
- [45] E. Wimmer, H. Krakauer, M. Weinert, and A. J. Freeman, *Phys. Rev. B* **24**, 864 (1981).
- [46] M. Weinert, E. Wimmer, and A. J. Freeman, *Phys. Rev. B* **26**, 4571 (1982).
- [47] [www.flapw.de](http://www.flapw.de).
- [48] S. H. Vosko, L. Wilk, and M. Nusair, *Can. J. Phys.* **58**, 1200 (1980).
- [49] P. Fischer, M. Polomska, I. Sosnowska, and M. Szymanski, *J. Phys. C* **13**, 1931 (1980).
- [50] I. Sosnowska, R. Przeniosło, P. Fischer, and V. Murashov, *J. Magn. Magn. Mater.* **160**, 384 (1996).
- [51] Z. Xu, J. Wen, T. Berlijn, P. M. Gehring, C. Stock, M. B. Stone, W. Ku, G. Gu, S. M. Shapiro, R. J. Birgeneau, and G. Xu, *Phys. Rev. B* **86**, 174419 (2012).
- [52] A. Mackintosh and O. Andersen, *Electrons at the Fermi Surface*, edited by M. Springford (Cambridge University Press, London, 1980), p. 149.
- [53] A. Oswald, R. Zeller, P. J. Braspenning, and P. H. Dederichs, *J. Phys. F* **15**, 193 (1985).
- [54] E. Simon, K. Palotás, L. Rózsa, L. Udvardi, and L. Szunyogh, *Phys. Rev. B* **90**, 094410 (2014).
- [55] B. Dupé, G. Bihlmayer, M. Böttcher, S. Blügel, and S. Heinze, *Nat. Commun.* **7**, 11779 (2016).
- [56] S. Meyer, M. Perini, S. von Malottki, A. Kubetzka, R. Wiesendanger, K. von Bergmann, and S. Heinze, *Nat. Commun.* **10**, 3823 (2019).
- [57] L. Desplat, S. Meyer, J. Bouaziz, P. M. Buhl, S. Lounis, B. Dupé, and P. A. Hervieux, [arXiv:2011.12055](https://arxiv.org/abs/2011.12055).
- [58] J. Jeong, E. A. Goremychkin, T. Guidi, K. Nakajima, G. S. Jeon, S.-A. Kim, S. Furukawa, Y. B. Kim, S. Lee, V. Kiryukhin, S.-W. Cheong, and J.-G. Park, *Phys. Rev. Lett.* **108**, 077202 (2012).
- [59] A. K. Zvezdin and A. P. Pyatakov, *Europhys. Lett.* **99**, 57003 (2012).
- [60] In the  $R\bar{3}c$  phase, the DMI contribution induced by our spin spiral from each Fe-O-Fe pair is in fact nonzero, but summation over six neighboring Fe pairs would result in an almost exact cancellation.
- [61] <https://www.archer2.ac.uk>.